Faraday Discussions

PAPER

Quantification of the effect of ultrasound in PEM water electrolyser with operando neutron imaging and numerical simulations

Stratis Trachanias*[a], Tamara Miličić [b], Wenyu Zhao[c], Xiaotong Ma[d], Yuzhe Fan[d], Tobias Arlt[e], Jayanath C. P. Koliyadu[f], Patrik Vagovic[f], Nikolay Kardjilov[e], Ingo Manke[e], Jakobus Hoffman[g], Anastasios Georgoulas[h], Alessandro Tegattini[i], Lukas Helfen[i], Bratislav Lukić[i], Claus-Dieter Ohl[d], Tanja Vidaković-Koch[b], Ioannis Karathanassis[a] and Manolis Gavaises[a,d]

Received 29th June 2026, Accepted 13th July 2026
DOI: 10.1039/x0xx00000x

This study investigates the effect of ultrasound (US) on the electrochemical performance and two-phase flow regimes within a custom-designed polymer electrolyte membrane water electrolyser (PEMWE) cell. The electrolyser cell was equipped with a US transducer-receiver pair that allowed US propagation through the active area. Operando neutron imaging experiments were conducted at the Institut Laue-Langevin (ILL), utilizing both in-plane and through-plane radiography to quantify water thickness as a proxy for gas distributions across different electrolyser components under varying operating conditions. Simultaneously, real-time monitoring of electrochemical performance was carried out, with a goal of identifying the effect of two-phase mass transport conditions on PEMWE losses. The results reveal a non-monotonic dependence of the US effect on current density and the flow regime that emerges in the flow channels. At intermediate current densities (~1000 mA cm^{-2}), US induces a measurable reduction in cell voltage, correlated with increased water occupancy in the flow channels, consistent with enhanced gas removal. In contrast, at high current densities (~6000 mA cm^{-2}), US leads to reduced water content in the channels and a deterioration in cell performance, suggesting a transition in the governing two-phase flow regime. CFD simulations of the baseline flow field support the experimental observations by identifying the presence of slug flow under these conditions.

Introduction

The pursuit of net-zero carbon targets has intensified global efforts to develop large-scale renewable energy storage and conversion technologies. Green hydrogen produced through water electrolysis powered by renewable energy has emerged as a genuine alternative to fossil fuels in sectors undergoing defossilisation, including the hard-to-abate transport sector[1] and iron and steel manufacturing. At the same time, green hydrogen is a promising option for long-duration energy storage[2,3]. With the large capacities that must be deployed in the coming years, careful design of the electrolyser cell, stack, and supporting systems is essential to lower both investment and operating costs of the overall plant. The latter are largely driven by the cost of electricity per kilogram of hydrogen produced. As a result, even small improvements in hydrogen production efficiency can lead to significant reductions in operating expenses.

PEMWE is a promising technology for green hydrogen production due to its high efficiency and excellent dynamic response compared to today's industry standard, alkaline electrolysers. However, its performance is limited by several factors, most notably two-phase transport, which introduces additional losses. The gas-evolving half-reactions generate a two-phase flow of water and oxygen in the anode compartment and water and hydrogen in the cathode compartment. Mass-transport losses arise primarily from inefficient gas removal at catalyst sites. Accumulated gas increases the local O_2 and H_2 concentrations in the ionomer surrounding the catalyst, leading to concentration overpotentials[4–6]. Furthermore, the gas bubbles can block the catalyst surface. In such a case, the reactant is considered not to be able to reach the active sites covered by gas, and consequently, bubble overpotential occurs[7–9]. On the anode side of the PEMWE, where water is the reactant, both of these mechanisms can take place,

[a] School of Science & Technology, City St George's, University of London, United Kingdom.
[b] Electrochemical Energy Conversion (EEC), Max Planck Institute for Dynamics of Complex Technical Systems, Magdeburg, Germany.
[c] AAU Energy, Aalborg University, Aalborg, Denmark.
[d] Otto von Guericke University, Magdeburg, Germany.
[e] Helmholtz-Zentrum Berlin für Materialien und Energie GmbH, Berlin, Germany.
[f] Center for Free-Electron Laser Science (CFEL), Deutsches Elektronen-Synchrotron (DESY), Hamburg, Germany
[g] South African Nuclear Energy Corporation (Necsa), Pretoria, South Africa.
[h] Liverpool Logistics Offshore and Marine (LOOM) Research Institute, School of Engineering, Liverpool John Moores University, United Kingdom.
[i] Institut Laue-Langevin, Grenoble, France.
*Corresponding author stratis.trachanias@citystgeorges.ac.uk

causing the overall mass transport overpotential. To mitigate this energy loss, most research focuses on optimising the porous transport layer (PTL). PTL is a porous structure that provides electrical contact to the catalyst layer while simultaneously creating pathways for water supply and oxygen removal. This counter-current transport of water and oxygen through the PTL was often considered the main bottleneck for the mass transport in PEMWE, causing significant mass transport losses[10]. The flow in the PTL was identified to be capillary driven and therefore determined by its properties, such as its thickness, porosity, and pore size distribution. Furthermore, the two-phase flow in the anode flow fields was also often studied[11]. Depending on their design and operating conditions, different flow regimes were observed, ranging from bubbly to annular flow. As a consequence, reactant availability at the catalyst layer is limited, and mass transport losses develop, especially at elevated current densities. In the literature, these limitations are commonly addressed through design-oriented strategies, such as optimized flow-field geometries and PTL designs that facilitate efficient gas removal while maintaining sufficient water supply.

In addition to the design-based approaches, sono-electrochemistry may offer a promising alternative pathway to mitigate mass-transport-related bottlenecks. Applying an ultrasonic field (US) induces a variety of acoustophoretic effects that are of potential relevance to gas-evolving electrodes, where bubbles nucleate, grow, and detach. Among the primary mechanisms that govern bubble dynamics under ultrasonic conditions are rectified diffusion, acoustic microstreaming[12] and Bjerknes forces[15]. The first effect refers to the isotropic oscillation of a bubble radius. During the high-pressure phase, the bubble contracts and internal gas concentration increases, driving gas diffusion out of the bubble. Conversely, during the low-pressure phase, the bubble expands and internal concentration drops, drawing gas in from the surrounding liquid. Because the bubble's surface area is larger during expansion, more gas enters than exits over a single cycle, resulting in a net increase in bubble volume over time. The oscillating bubble in a viscous liquid creates besides an oscillating flow also a steady flow. The latter phenomenon is called microstreaming and depends on the acoustic frequency, amplitude, and size of the bubbles[13]. In addition, the pressure gradients of the acoustic field may be attractive and repulsive to oscillating bubbles. Particularly, the acoustic emission of equal sized bubbles leads to an attractive force enhancing coalescence and thus easier detachment from the electrodes. Overall, these effects lead to improved mass and heat transport. To maximize them, the ultrasonic field is typically operated close to the bubble's volumetric resonance, known as the Minnaert frequency[14].

Previous studies have demonstrated the positive effects of ultrasound (US) on mass transport in water electrolysers. For example, Pollet et al[16] found that power US did not dramatically change the mechanism of the hydrogen evolution reaction (HER), but instead increased currents at the Pt surface area through effective hydrogen bubble removal into the bulk electrolyte. Similarly, Forounghi et al[17] noted that ultrasonication facilitates gas bubble detachment from active sites, freeing them for further reactions. Recently, reduction of ohmic losses was demonstrated by vibrating the electrode that leads to clearing of the electrode from bubbles through acoustically forced coalescence. However, these studies primarily focused on electrolytic bubbles generated in an unconfined bulk electrolyte, where buoyancy is the primary departure force. In confined porous geometries, such as the PTLs and flow channels of a commercial electrolyser cell, the forces governing bubble departure and the resulting two-phase flow regimes remain poorly understood.

To thoroughly investigate this phenomenon, we employed neutron imaging, which offers the distinct advantage over optical imaging of quantifying the exact amount of water within the visualization region[18]. Selamet et al[19] were the first to employ this simultaneous neutron radiography and optical imaging to investigate the effect of cathode water accumulation with and without N_2 purging. Since then, many groups have employed the technique for several investigations in PEMWE[20–24]. In this study, we combine electrochemical measurements, operando neutron imaging, and computational fluid dynamics (CFD) simulations to elucidate bubble dynamics in PEMWE and evaluate the application of US. Importantly, the numerical environment allows for the exploration of bubble dynamics under reduced gravitational environments, where buoyancy-driven bubble detachment is suppressed, a critical factor for electrolysers designed for space applications. To the authors' best knowledge, this is the first work to investigate US irradiation in the PEMWE system through combined operando electrochemical characterisation and neutron imaging.

Materials and Methods

Cell Description

The electrolyser cell used in the experimental investigation is shown in Figure 1. Commercial components were used: Ion Power catalyst-coated membrane (CCM, Nafion 117 membrane, 1.0 mg cm^{-2} IrOx as the anode catalyst layer, and 0.3 mg cm^{-2} Pt as the cathode catalyst layer), platinized titanium porous transport layer (PTL) from Bekaert (2GDL20-1,0 - 1 mm thickness, 77% porosity), and carbon-based gas diffusion layer (GDL) from Freudenberg (H24C5). However, the cell was specially designed to allow simultaneous application of US and neutron imaging. Aluminium 6060 was chosen as the material of flow fields, end plates, and piezo plates due to its low neutron attenuation. The flow fields were coated with gold (2-4 µm, 70 HV fine gold, nickel as an intermediate layer) to protect aluminium from corrosion under anodic water electrolysis conditions. The flow fields had a parallel channel design, with 3 channels of 1 x 1 mm^2 cross-sectional area, 40 mm length, and 1 mm wide land between every two channels, as depicted in Figure 4. The application of US required positioning of the piezo elements (US transducer/receiver pair) close to the

two-phase flow. Thus, the cell was designed in a bone-like shape, with a narrow middle section (15 mm width, 40 mm length, and 17.67 mm thickness) and large top and bottom sections (40 mm width, 40 mm length, and 37.67 mm thickness). While the top and bottom sections accommodated the inlet/outlet connections, current connectors (made directly to the flow fields), and compression bolts (M4 stainless steel, four in the top and four in the bottom section), the middle section contained the active area of 5 x 20 mm^2 positioned in the middle of the flow fields. The same section bore two piezo elements (20 mm diameter, 2 mm thickness, PZT4, 1 MHz thickness resonance frequency, Beijing Quanxin Ultrasonic Co.): the one on the anodic side of the cell used as a US transducer and the one on the cathodic side of the cell used as the US receiver/sensor. The US transducer/receiver pair was held in place with the help of two piezo plates compressed with four bolts (M4 stainless steel). To allow electrical connections

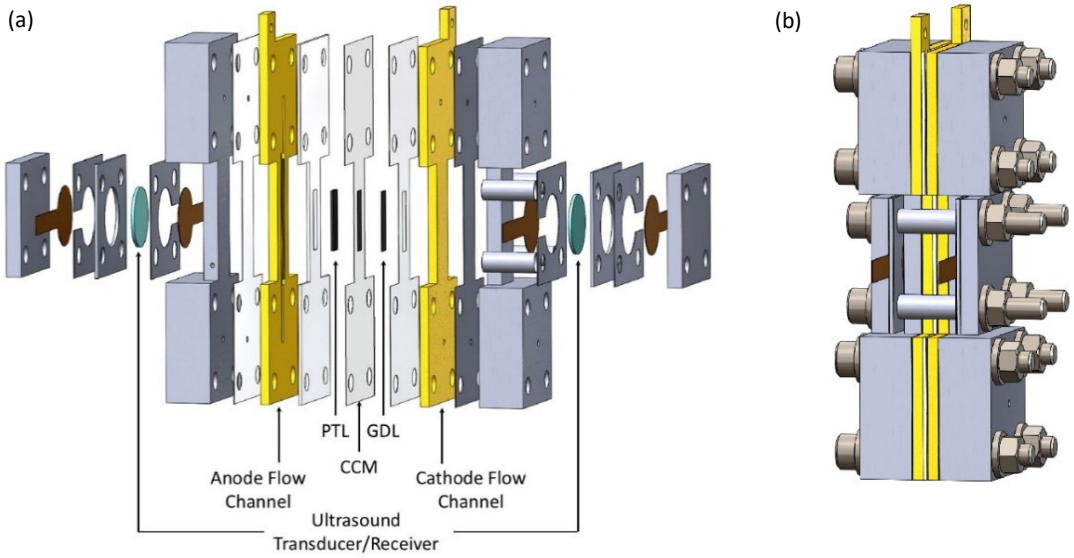

Figure 1 (a) Volume rendering and exploded view of the electrolysis cell. From the outer to the inner of the cell: piezo plate, ultrasound transducer/receiver pair with two copper sheets and positioning gaskets, end plate, flow field, PTL/GDL with gasket, and CCM. (b) Assembled electrolysis cell.

to the US transducer and receiver, two copper sheets (0.25 mm) were used for each. The positioning of the US elements and copper sheets was achieved with Teflon gaskets (Reichelt Chemietechnik) of appropriate thicknesses. Teflon gaskets were also used around PTL and GDL for positioning them, sealing the cell, and electrical isolation of the flow fields from the end plates. On the other hand, the end plates and piezo plates were isolated with Kapton tape to prevent electrical contact between the transducer elements and the cell. The piezo plates had an opening in the middle for sensing the temperature of the US transducer/receiver. Also, an opening in the anode end plate was made below the active area for recording the cell temperature. The cell was assembled with a 2.5 Nm torque. To ensure no short circuit can happen, polyether ether ketone (PEEK) pipes and PEEK spacers were used to isolate the bolts.

Setup Description

A typical test bench for PEMWE was used (Figure 2). The water was supplied to the anode compartment from the inlet reservoir (B in Figure 2) by a gear pump (ISMATEC MCP-Z, P in Figure 2). The water was preheated in the inlet reservoir by passing warm oil from the thermostat (F32, Julabo, TC in Figure 2) through the reservoir jacket. The flow rate of water was maintained at 3.25 or 10 ml min^{-1} during the measurements. The anode outlet stream was recycled to the inlet reservoir, which was open, allowing the produced oxygen and water vapor to escape. The cathode side was purged with nitrogen at room temperature and 9 ml min^{-1}, set by a mass flow controller (Bronkhorst, EL-FLOW Select, FIC in Figure 2). After passing the electrolyser, the exit stream from the cathode side was directed to the gas-liquid separator (air-cooled condenser, LGS in Figure 2). The condensed water was occasionally removed from the separator, while the gas stream was connected to the gas exhaust-recuperation system. A Pt-100 sensor (TC Mess- und Regeltechnik GmbH, TI4 in Figure 2) was positioned in the anode end plate to monitor the cell temperature. Additionally, 5 Type K temperature sensors (TC Mess- und Regeltechnik GmbH, TI1-3 and TI5-6 in Figure 2) were placed in the anode inlet and outlet streams, cathode outlet stream, and piezo plates. The anode outlet temperature sensor was considered representative of the electrolyser (or CCM) temperature, and this temperature was manually regulated to the desired temperature (30, 40, or 60°C ± 1°C). This was achieved by adjusting the thermostat temperature and the power of the heating foils. Four silicon heating foils (Friedr. Freek, Silikon-FLHK 24 V/15 W) were used; two were attached to the top and two to the bottom section of the electrolyser. Furthermore, the setup had two automatic valves (V in Figure 2): one between the inlet reservoir and the pump, and the second at the cathode outlet liquid stream. The setup had an in-house-built control box using Siemens WinCC software, enabling remote control and allowing uninterrupted neutron imaging. Electrochemical measurements were performed with Ivium

XP40 potentiostat/galvanostat (PG in Figure 2) that allowed currents up to ±40 A and voltages up to ±10 V. IviumSoft was used to control the potentiostat, and IviLab was used to extract the data. Finally, the US transducer was operated by a high-voltage power amplifier (AG 1021 Amplifier, T&C Power Conversion), in connection with the signal generator (RIGOL DG1022) used to generate a high-frequency voltage signal. The sensing piezo element (US receiver) was connected to an oscilloscope (RIGOL DHO814, OS in Figure 2).

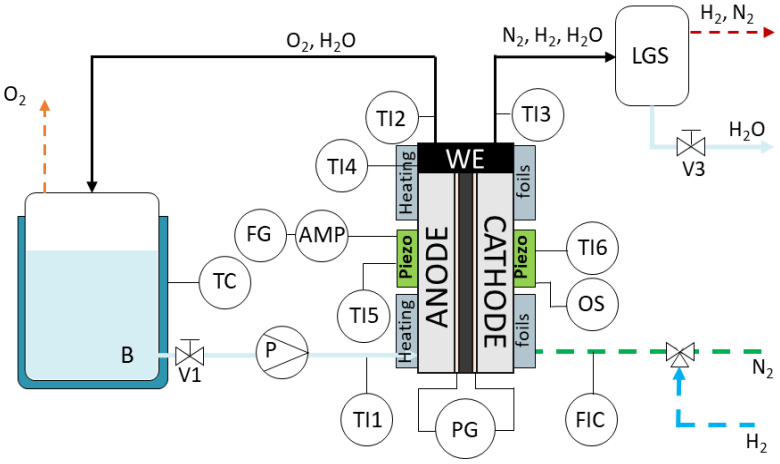

Figure 2 (a) Schematic representation of the experimental test bench: PEM water electrolysis test bench: AMP – voltage power amplifier, B – inlet water reservoir, FIC – volumetric flow indicator and controller, FG – frequency generator, LGS – liquid-gas separator, OS – oscilloscope, P – pump, PG –potentiostat/galvanostat, Piezo – ultrasound transducer/receiver pair, TI – temperature sensor, TC – thermostat, V – automatic valve, WE – water electrolyser, O_2 - oxygen, H_2O - water, H_2 - hydrogen, N_2 - nitrogen.

Design of experiment

Three electrolysers of the same structure were investigated at different temperatures (30°C, 40°C, and 60°C) and anode inlet water flow rates (3.25 ml min^{-1} and 10 ml min^{-1}). US effect was tested at five distinct current densities: 10, 100, 1000, 3000, and 6000 mA cm^{-2}. Operando neutron imaging was performed at the Institut Laue-Langevin (ILL) in Grenoble, France, while the measurement reproducibility was proved by repeating the US and electrochemical analysis at the Max Planck Institute (MPI) in Magdeburg, Germany. Two cells were operated at ILL (WE1 for in-plane imaging and WE2 for through-plane imaging), and one cell was measured at MPI (WE3). The details of the measurements and associated data analysis are explained below.

Ultrasound measurements

The same protocol for analysis of the US effect was applied at ILL and MPI for all experimental conditions. The operation was initially conducted under steady-state (SS) galvanostatic conditions (no US - silent), followed by galvanostatic operation with US burst operation at different frequencies. First, a US sweep is performed in the frequency range of 50 to 150 kHz to identify the resonance frequencies of the system. An example of the resulting signal recorded on the oscilloscope, with the dominant peaks at 91 kHz and 98 kHz, is shown in Figure 3a. Then, a duty cycle of 2 s was chosen for a US burst mode at the identified system resonant frequencies. The US pulse duration was set to 50,000 cycles. E.g., for frequency 91 kHz, the US pulse lasted 0.549 s, and it was repeating every 2 s (Figure 3b). The loading power supplied to the US transducer during the burst was between 4 and 15 W cm^{-2} (or 1.10 and 4.12 W cm^{-2} averaged over the 2 s interval), depending on the operating conditions and US frequency. This procedure was repeated for different current densities, temperatures, flow rates, and different cells.

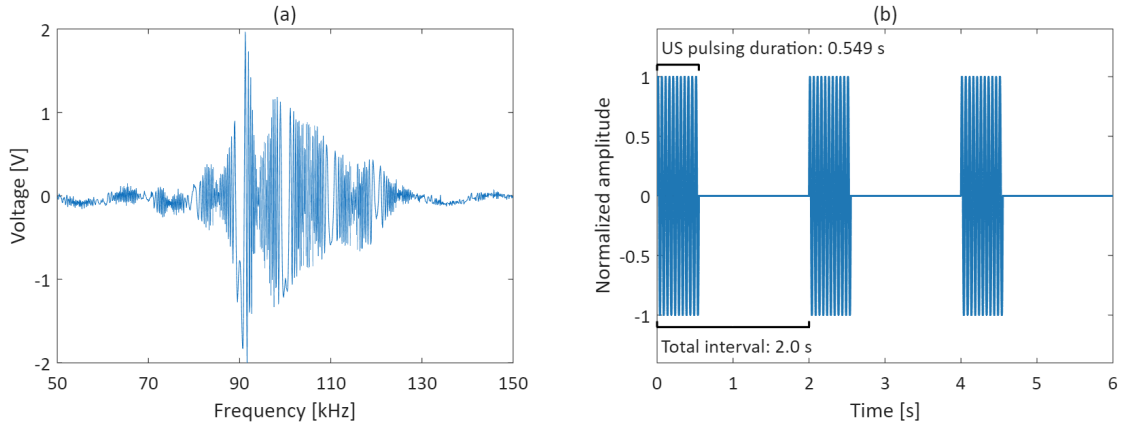

Figure 3 (a) Frequency sweep measurement for the determination of the system resonant frequencies. (b) Schematic representation of the ultrasound burst protocol used for studying the effect of the ultrasound on electrolyser performance.

Electrochemical Diagnosis

To evaluate the performance of the electrolysers containing different PTLs at different operating conditions, polarization curves were measured. Consecutive galvanostatic holds were performed in the current range of 0-9 A cm^{-2}, each for a duration of 2 min. The voltage of the last 10 s of the galvanostatic hold was averaged and used to construct the polarization curve. After each galvanostatic step, high-frequency resistance (HFR) was determined with electrochemical impedance spectroscopy (EIS) measurement. EIS was performed between 100 Hz and 100 kHz with 10% of the SS current as the amplitude. The measured voltage and HFR were used to calculate the IR-free voltage as:

$$U_{IR} = U - iR_{ohm},$$

where $\boldsymbol{U}$ is the total cell voltage (V), $\boldsymbol{i}$ current density (A cm^{-2}), and $\boldsymbol{R_{ohm}}$ ohmic resistance (HFR, Ω). The obtained IR-free voltage was used to construct the IR-free polarization curve ($\boldsymbol{U_{IR}}$ *vs* $\mathbf{log}(\boldsymbol{i})$).

Neutron Imaging

Imaging was performed at the cold neutron micro-tomography instrument, PorTo, at ILL. The ILL reactor provides the highest-intensity continuous neutron flux in the world, which at the PorTo amounts to $3.2 \cdot 10^8$ n cm^{-2} s^{-1} (at reactor power of 58 MW), allowing high-resolution imaging at good temporal resolution. For these measurements, a pinhole with a 30 mm diameter was employed and a high-resolution detector combining a 20 µm gadolinium oxide powder scintillator on a 200 µm thick aluminium substrate, an XR-Heliflex 50 mm f./1.0 (Rodenstock) objective lens, and a 50 mm f./1.2 Canon imaging lens attached to the Hamamatsu ORCA-Flash V3 sCMOS camera. This combination of pinhole and detector system resulted in an effective pixel size of 6.5 µm, a field of view of 13.3 × 13.3 mm^2, and a temporal resolution of 0.25 s. This allowed a proper visualisation of the water thickness in the electrolysis cell, as well as bubble dynamics.

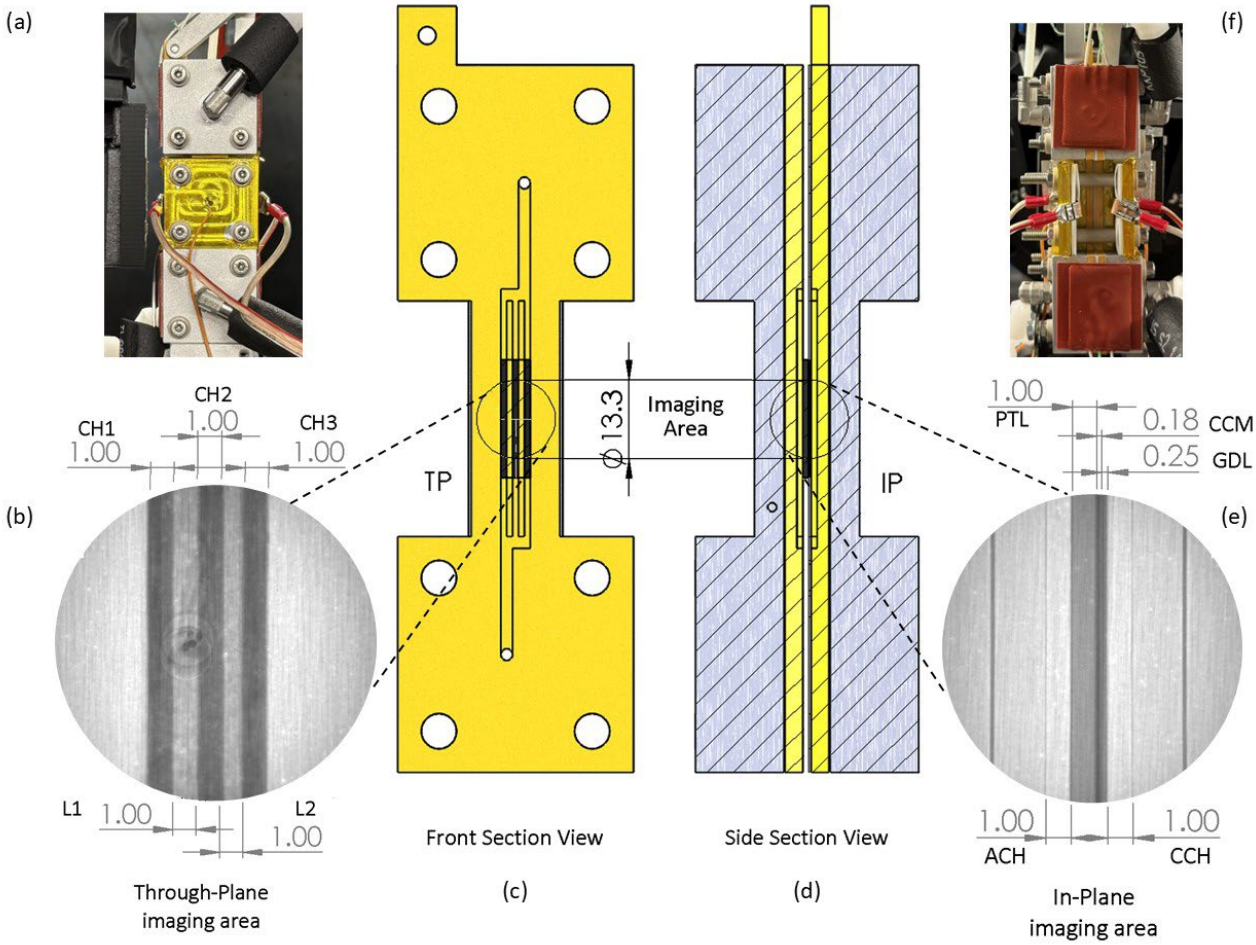

Figure 4. Through-plane (TP) imaging (a-c) and in-plane (IP) imaging (d-f): position of the electrolyser in the beam (a,f), obtained TP and IP grey-scale images (b,e), and schematics of the TP and IP views of electrolysers with imaging area marked (c,d). All dimensions are given in mm. ACH – anode flow channels, CCH – cathode flow channels, CCM – catalyst-coated membrane, CH – channel, GDL – gas diffusion layer, L – land, PTL – porous transport layer.

Both through-plane (TP, beam directed perpendicular to the active area) and in-plane (IP, beam passing parallel to the active area) radiographies were performed, capturing the water thickness profiles along the different flow channels and along different electrolyser regions, respectively. Only the middle part of the active area in between the US elements was captured. Figure 4 explains the IP and TP imaging, showing the position of the electrolyser in the beam, the area that is imaged, as well as the obtained images of the electrolyser.

The imaging protocol commenced by taking the reference images. Firstly, dark fields (DFs) were imaged without a neutron beam. Next, the electrolyser was heated to the operating temperature, and dry images (DIs) were taken with the electrolyser in the beam before water was introduced and cell operation started. Both DFs and DIs were taken for 1 min, resulting in a total of 240 images. In the next step, water circulation through the cell was activated to humidify it. At the same time, the nitrogen purge was activated. Humidification was conducted for approximately 1 hour under open-circuit-voltage (OCV) conditions, followed by a short preconditioning at 3000 mA cm^{-2} for a duration of 1-2 hours. Finally, the electrolysis operation at the first investigated temperature and inlet water flow rate was initiated. The analysis consisted of polarization curve measurement and SS galvanostatic holds at different current densities during silent and US conditions. The exact procedure for these measurements was described in the previous sections. Imaging was performed only during galvanostatic holds. One set of images was taken during the hold, once the SS response was achieved for a duration of 2 min resulting in 480 images. The second set of images was taken during the SS operation with the US (also for a duration of 2 min giving 480 images). The described analysis, including polarization curve measurement and galvanostatic holds, was repeated for different temperatures and anode inlet water flow rates. The change in these variables required a stabilization period of 1-2 hours. No imaging was performed during this time.

The obtained images were used to determine water thickness profiles of the electrolyser. This required several post-processing operations on images as described below. Image processing was done with Fiji ImageJ (Version 2.14.0/1.54p). First, the median images from the DFs and DIs stacks were calculated. The alignment of the DI median and operating images (OI) was verified, and when necessary, the DI was translated and/or rotated. The obtained medians were employed to correct the operating image (OI).

$$\mathrm{M} = \frac{\mathrm{OI}-\mathrm{DF}}{\mathrm{DI}-\mathrm{DF}}.$$

The corrected image, M, contains only information about the water amount. Thus, the Beer-Lambert law was applied to calculate the water thickness of the electrolyte from the corrected image:

$$d_{H_2O} = \frac{\ln(\mathrm{M})}{-\mu_{H_2O}},$$

where $\mu_{H_2O} = 0.5$ mm^{-1} is the water attenuation coefficient[20,25] for cold neutrons. Scattering was assumed to be negligible and was therefore not corrected. The large pinhole was used to maximize neutron flux, and the sample-to-detector distance was minimized to limit the contribution of scattered neutrons to the images.

After this, the median projection was calculated to obtain the average water thickness profile along the x-axis relative to the detector. In addition to the overall profiles, profiles of different regions of interest (ROIs) were determined. For IP images, these are the anode flow channels (ACH), PTL, CCM, GDL, and cathode flow channels (CCH). On the other hand, the ROIs for the TP images that were considered were the three channels (CH1-3) and two lands (L1-2). These ROIs are marked in Figure 4.

CFD Model Description

To complement our experimental results and provide insight into the two-phase flow regimes that emerge in our test electrolysis cell, computational fluid dynamics (CFD) simulations were performed. These simulations model the anode flow channel to predict bubble dynamics and extract time-averaged water thickness profiles, which are then compared with the experimental results.

The volume of fluid (VoF) method[26], is employed to capture the two-phase flow, using the geometric sharp interface advection scheme developed by Roenby et al.[27]. This approach is well-established in the literature for modelling multiphase phenomena in PEMWEs[28–33]. The incompressible momentum equation includes in its right hand side a gravitational body force F_b and a surface tension force F_{St} term for the oxygen bubbles in water, utilizing the continuum surface force (CSF) approximation by Brackbill et al.[34] The continuity, momentum, and volume fraction advection equations are expressed respectively as:

$$\nabla \cdot \mathbf{U} = 0$$

$$\frac{\partial(\rho\mathbf{U})}{\partial t} + \nabla \cdot (\rho\mathbf{U} \otimes \mathbf{U}) = -\nabla p + \nabla \cdot [\eta(\nabla\mathbf{U} + \nabla\mathbf{U}^{\mathrm{T}})] + F_b + F_{St}$$

$$\frac{\partial a}{\partial t} + \nabla \cdot (a\mathbf{U}) = 0$$

where the mixture density and viscosity are defined as: $\rho = \alpha\rho_{H_2O} + (1-\alpha)\rho_{O_2}$ and $\eta = \alpha\eta_{H_2O} + (1-\alpha)\eta_{O_2}$.

To reduce the complexity of the modelling and to account only for the transport phenomena of the flow, the following assumptions are made, in agreement with the work by Dang et al[32].

- Oxygen flux is considered constant at the PTL, indicating a constant and uniform current density.
- Gas crossover through the PEM is assumed negligible because the membrane has low gas permeability and the anode and cathode are operated at equal (near-ambient) pressure, eliminating pressure-driven permeation.
- The flow in the incoming channels and the porous media is considered laminar due to low inlet velocity and subsequent low Reynolds number.
- The phase change of water and the dissolution of oxygen gas are ignored.
- The process is considered isothermal. Thus, the energy equation is omitted.

The flux of oxygen gas generated should satisfy the Faraday equation:

$$\dot{m}_{O_2} = \frac{jS}{4F} M_{O_2},$$

where $\dot{m}_{O_2}$ is the mass flow rate of the gas in $\mathrm{kg\ s^{-1}}$, j is the applied current density in $\mathrm{A\ cm^{-2}}$, S the effective active area in $\mathrm{cm^2}$, F the Faraday constant in $\mathrm{C\ mol^{-1}}$, and M_{O_2} the molar mass of O_2 in $\mathrm{kg\ mol^{-1}}$.

The produced gas is injected into the flow field through 258 holes distributed at the intersection of the flow channel and the PTL, imitating the nucleation points where bubbles emerge along the PTL surface. The flow field is meshed with 6,160,384 hexahedral elements of size 31.25 µm, resulting in a high-resolution mesh for our simulations. The model does not include acoustic forcing and therefore represents baseline flow conditions without US. The model is validated against the experimental measurments with the time averaged water thickness along the height of the three channels in the imagging area of WE3 operating at 30°C with a flow rate of 10 ml $\mathrm{min^{-1}}$ and a current density of 6000 mA $\mathrm{cm^{-2}}$ as shown in Figure 5.

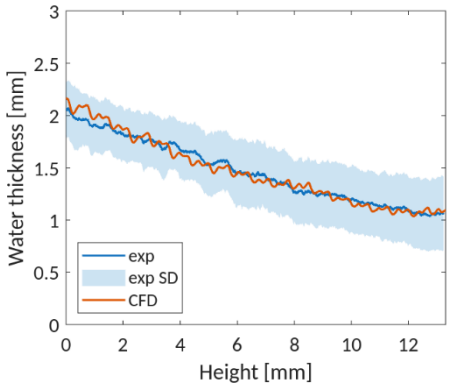

Figure 5. Validation of the CFD model with the time averaged water thickness along the height of the three channels in the imaging area. Operation of WE3 at 30°C with a flow rate of 10 ml $\mathrm{min^{-1}}$ and at a current density of 6000 mA $\mathrm{cm^{-2}}$.

Results and Discussion

Effect of ultrasound on voltage response

The application of the US in pulsed mode resulted in periodic changes in output voltage, as shown in Figure 6a for the electrolyser operated at MPI (WE3) at 30°C, atmospheric pressure, and 1000 mA $\mathrm{cm^{-2}}$. During the US excitation at 91 kHz (0.549 s), a sharp voltage drop was observed. For the rest of the period (1.451 s), when no US was supplied, the voltage slowly increased to the previous value. However, before reaching it, the next burst would start, and the voltage would drop again. The amplitude of these oscillations was dependent on the power supplied to the piezo elements, but also on SS current density, temperature, and inlet water flow rate. Evidently, the voltage decreases monotonically during the US excitation (Figure 6a). Additionally, transient behaviour was observed, with an exponential drop in voltage occurring when the US excitation started, and an exponential increase in voltage occurring upon US pulsing (Figure 6b, original data). The linear drift in voltage was attributed to an increase in electrolyser temperature due to heating up of the piezo elements (Figure 6c). On the other hand, the transients are believed to be caused by the US itself.

To evaluate the effect of the US on electrolyser performance, the observed drift in voltage was first removed by linearly fitting the US-affected voltage (only the part of the signal that showed a purely linear trend, without the exponential changes) and subtracting the slope from the voltage data (Figure 6b, corrected data). In this way, the effect of electrolyser temperature increase during US pulsing was removed. Verification of this assumption was done by comparing the measured SS voltage change before and after the US pulsing (Figure 6b) with the voltage change calculated based on the measured temperature change (Figure 6c). The latter was determined assuming a negligible effect of the temperature on kinetics. The effect of temperature on the open-circuit voltage (OCV, U_{ocv}, V) was captured by correlation[35]:

$$U_{ocv} = 1.229 - 0.9 \cdot 10^{-3}\left(T_{A,out} - 298\right),$$

where $T_{A,out}$ is the anode outlet temperature.

Ohmic resistance dependence on temperature was taken into account as follows[35]:

$$R_{ohm} = d_m \left[(0.005139\lambda_m - 0.00326) \exp\left(1268\left(\frac{1}{303} - \frac{1}{T_{A,out}}\right)\right)\right]^{-1} \text{ S cm}^{-2},$$

where d_m is membrane thickness (183 μm) and λ_m is membrane conductivity (assumed to be 14, independent of operating conditions).

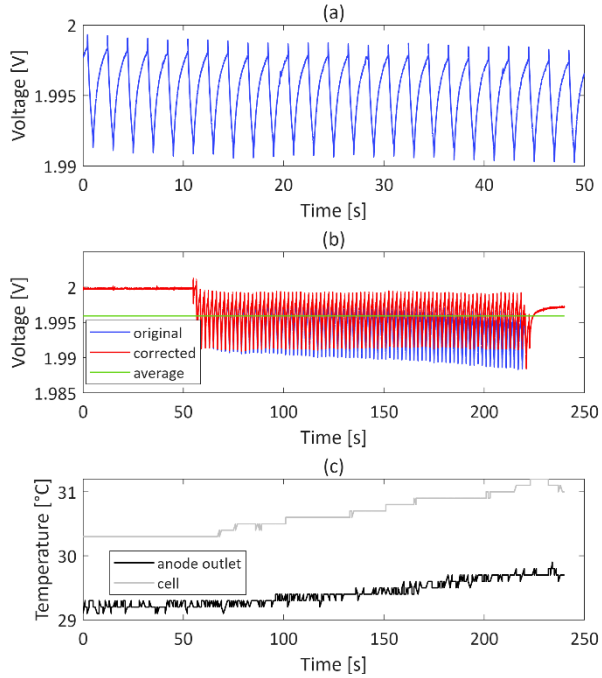

Figure 6 (a) Raw data showing the voltage oscillations during US burst. (b) Voltage time profiles: original data, data corrected for the linear drift, and mean value of voltage during US excitation. (c) Temperature profiles measured in the end plate and anode outlet. The measurements were performed on WE3 at 30°C, 3.25 ml min^{-1} water flow rate, and 1000 mA cm^{-2} current density. Ultrasound at a frequency of 91 kHz and with a loading power of 7 W cm^{-2} (corresponding to 1.92 W cm^{-2} normalized to the whole pulse interval) was supplied.

Using the data shown in Figure 6, the measured drop in SS voltage due to US is 2.59 mV. The calculated voltage drop based on the measured temperature increase of 0.5°C is 2.3 mV. Since the calculated and measured voltage drop values are in good agreement, it is justifiable to assume that the linear drift is indeed due to the increase in temperature during US pulsing, and the correction of the linear drift is appropriate. Only after this was the average voltage value during US pulsing calculated and compared with the SS voltage (galvanostatic hold without US pulsing). For the data in Figure 6, it was calculated that the average voltage during US excitation is 3.88 mV smaller than in the steady state (before the US excitation). Thus, in this way, the US effect was isolated from the effect of temperature increase. For the given case, the US was found to reduce voltage compared to the SS operation. Furthermore, the power consumption during SS and US operation can be calculated by multiplying the time signals of current and voltage and averaging them. The SS signal before the US excitation and the US-affected signal without transients were considered relevant for the comparison. Using data in Figure 6, one calculates the power consumption of 2.000 W and 1.995 W cm^{-2} for steady-state and US operation, respectively. Thus, the US not only reduces voltage but also leads to lower power consumption (5 mW cm^{-2} reduction for this case). However, the reduction in power consumption is rather small and much smaller than the loading power of the US transducer (7 W cm^{-2} during the burst, corresponding to 1.92 W cm^{-2} on average for the whole interval). Two questions arise: 1) what phenomena are affected by the US during electrolyser operation that led to the observed power decrease, and 2) is the effect of the US dependent on the operating conditions. The following sections attempt to answer these questions.

Ultrasound effect at different current densities

Figure 7a depicts the US effect on voltage response at different current densities by analysing the difference between the average voltage during US pulsing and the SS voltage. This voltage difference is negative for a wide range of currents, indicating that the average voltage during US pulsing is smaller than the voltage in steady state. However, the US effect on voltage is nonlinearly dependent on current density. A maximal decrease in voltage due to US excitation is observed at 1000 mA cm^{-2}, with even a 3.61 mV decrease for WE2 and a 2.92 mV decrease for WE3, resulting in 4 and 3.6 mW cm^{-2} power consumption decrease,

respectively (power consumption data is presented in Figure S1, Supplementary Information). The lower current densities also showed lower voltages during US operation than in the steady state, but the decrease was of lower magnitude than at 1000 mA cm^{-2}. A similar trend was observed for the 3000 mA cm^{-2} current density. However, at 6000 mA cm^{-2}, the change in voltage was either negligible or even an increase in average voltage and power consumption during US pulsing in comparison to the SS voltage was observed. The high reproducibility of the measurements performed on the cells tested at ILL and MPI demonstrates the reliability of the results. Small quantitative differences likely come from the differences in the performance of the two cells (Figures S2a, S3-4), as well as the difference in US frequency (91 and 105 kHz for WE3 and WE2, respectively).

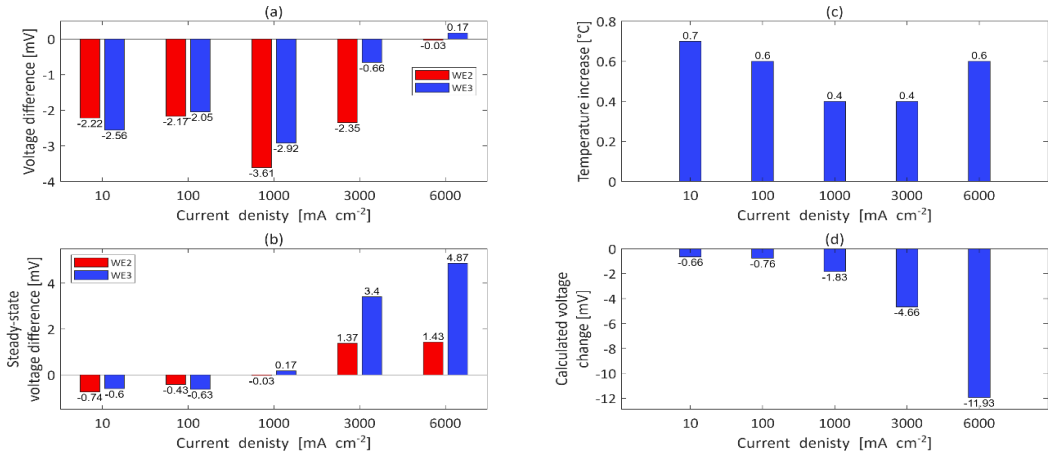

Figure 7 (a) Effect of current density on voltage difference without and with US excitation. (b) Steady-state voltage difference after and before US excitation at different current densities. (c) Increase in anode outlet temperature during US excitation at different current densities. (d) Calculated voltage changes due to the measured temperature increase at different current densities. The measurements were performed on WE2 and WE3 at 30°C and 10 ml min-1 water flow rate. US at frequencies of 91 kHz (WE3) and 105 kHz (WE2) and with a loading power of 6 (WE2) and 7 (WE3) W cm-2 (corresponding to 1.43 and 1.92 W cm-2 normalized to the whole pulse interval, respectively) was supplied.

From analysis of the SS voltage change during US pulsing (Figure 7b shows the difference between SS voltage after and before the pulsing), it is notable that for lower current densities (10 and 100 mA cm^{-2}), the SS voltage decreases during US pulsing (Figure 7b). The measured decrease corresponded well to the calculated voltage change (Figure 7d) based on the measured temperature increase (Figure 7c). Thus, the measured difference in SS voltage at low current densities could be attributed to the temperature increase. However, at 1000 mA cm^{-2} and higher currents, this is no longer the case. Under these conditions, the SS voltage increases (Figure 7b) despite the measured temperature increase (Figure 7c) that is expected to lead to the voltage decrease (Figure 7d). Especially interesting is the electrolyser behaviour at the highest current density (6000 mA cm^{-2}). As already mentioned, the US pulsing resulted in an increase in the average voltage and power consumption compared to steady state (Figure 7a). Furthermore, after US excitation, the SS voltage was higher than the initial SS voltage measured before US pulsing (a 4.87 mV increase was measured, as shown in Figure 7b). This voltage increase was present despite a temperature increase of 0.6 °C, equivalent to a voltage decrease of approximately 12 mV at 6000 mA cm^{-2} (Figure 7c-d). The observed behaviour is rather peculiar and is currently not sufficiently understood. However, at lower current densities, the US irradiation positively affects the electrolyser's performance, though the decrease in electrolyser power consumption is much smaller than the loading power of the US transducer. On the other hand, at high current densities, the US deteriorates the electrolyser performance, with indications of irreversible changes.

Previous studies have observed a more promising effect of ultrasonic treatment on the performance of water electrolysers. For example, Li et al.[36] have shown that the application of ultrasonic treatment in alkaline water electrolysers resulted in a reduction in cell voltage of up to 300 mV. The decrease in voltage was more pronounced as the current density increased. However, in the case of high electrolyte concentrations, it was independent of current density. In that study, the current density was limited to 400 mA cm^{-2}. The observed voltage decrease was attributed to a reduction in ohmic resistance due to improved bubble removal. This suggests that bubble removal is less important in the case of PEMWEs. This can be explained by the use of a solid electrolyte, which has low gas permeability and therefore its conductivity is less affected by the gas evolved at the anode and cathode, and perhaps by a more effective design of PEMWEs, resulting in a less pronounced mass transport issues and thus smaller influence of ultrasound on the voltage.

Influence of temperature and flow rate

Figure 8 shows the effect of temperature and inlet water flow rate on the electrolyser behaviour under US in comparison to the steady state. The decrease in inlet water flow rate was found to result in a larger effect of US on electrolyser performance: a larger voltage decrease during US pulsing was measured for lower inlet flow rate. The only exception was the voltage behaviour at the lowest current density measured, 10 mA cm^{-2}, which showed the opposite dependence on inlet water flow rate.

Furthermore, an increase in temperature resulted in a smaller voltage change during US operation in comparison to the steady state for all current densities. This is in agreement with the literature studies on alkaline water electrolysis[37,17], and in our work was true only for the current densities up to 3000 mA cm^{-2}, where a positive effect of the US was measured. On the other hand, for 6000 mA cm^{-2}, higher temperature resulted in a more pronounced performance deterioration during US pulsing. Analogous was observed for WE2 and depicted in Figure S8. The polarization measurements of the electrolysis cells show that, while temperature significantly affects voltage losses (the lower the temperature, the higher the voltage), the effect of the inlet water flow rate was not observed (Figures S2b-c, S5-7). In the case of temperature, it could be expected that electrolyser performance at a lower temperature, which results in higher voltage losses, will be more affected by US irradiation. However, the latter was also observed for the lower inlet flow rate, which seemingly doesn't affect the electrolyser performance.

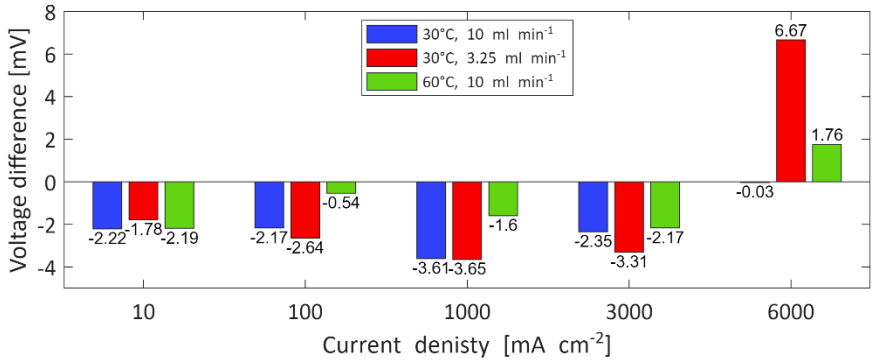

Figure 8. Influence of the temperature and flow rate on the difference in voltage without and with ultrasound excitation at different current densities. The measurements were performed on WE2 at 30 and 60 °C and 3.25 and 10 ml min^{-1} water flow rates. Ultrasound at a frequency of 105 kHz and with a loading power of 6 W cm^{-2} was supplied (corresponding to 1.43 W cm^{-2} normalized to the whole pulse interval).

Effect of ultrasound on water thickness profiles

The effect of the US is also visible on the time-averaged water thickness profiles. Figure 9 depicts the time- and height-averaged water thickness profiles from TP radiography for WE2 for the same operating condition discussed above (30°C with a flow rate of 3.25 ml min^{-1} and 1000 mA cm^{-2}). The US leads to an increase in the measured water thickness in the channels, meaning that water content is higher and consistent with enhanced gas removal. Additionally, Figure 10 depicts the time-averaged IP water thickness profiles for WE1 at higher current densities of (a) 3000 mA cm^{-2} and (b) 6000 mA cm^{-2}. As can be seen, the trend observed at low

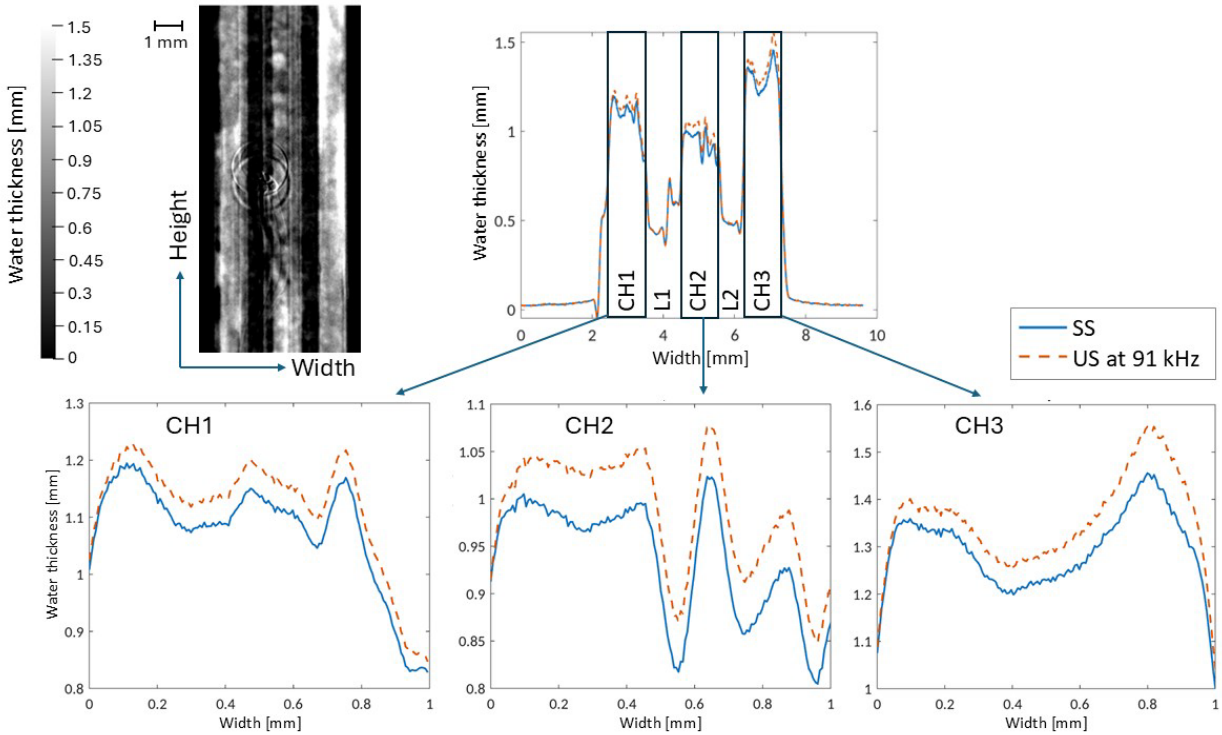

Figure 9. Comparative time-averaged TP water thickness profiles for WE2 for steady state and ultrasound pulsing at 91 kHz and loading power of 7 W cm^{-2} corresponding to 1.92 W cm^{-2} normalized to the whole pulse interval. The test cell was operated at 30°C, water flow rate of 3.25 ml min^{-1}, and a current density of 1000 mA cm^{-2}.

current density is still visible at 3000 mA cm^{-2}, but it reverses at 6000 mA cm^{-2}. These findings strongly indicate that the impact of the US is influenced by the prevailing two-phase flow regime. While at 3000 mA cm^{-2} an increase in overall water thickness of the anode channel was observed, indicating improved gas removal, the opposite is the case for operation at 6000 mA cm^{-2}. This is likely due to the fact that at 6000 mA cm^{-2}, a large amount of gas is produced and large slugs form in ACH. The US may be breaking up these slugs into smaller bubbles and, therefore, hindering their removal.

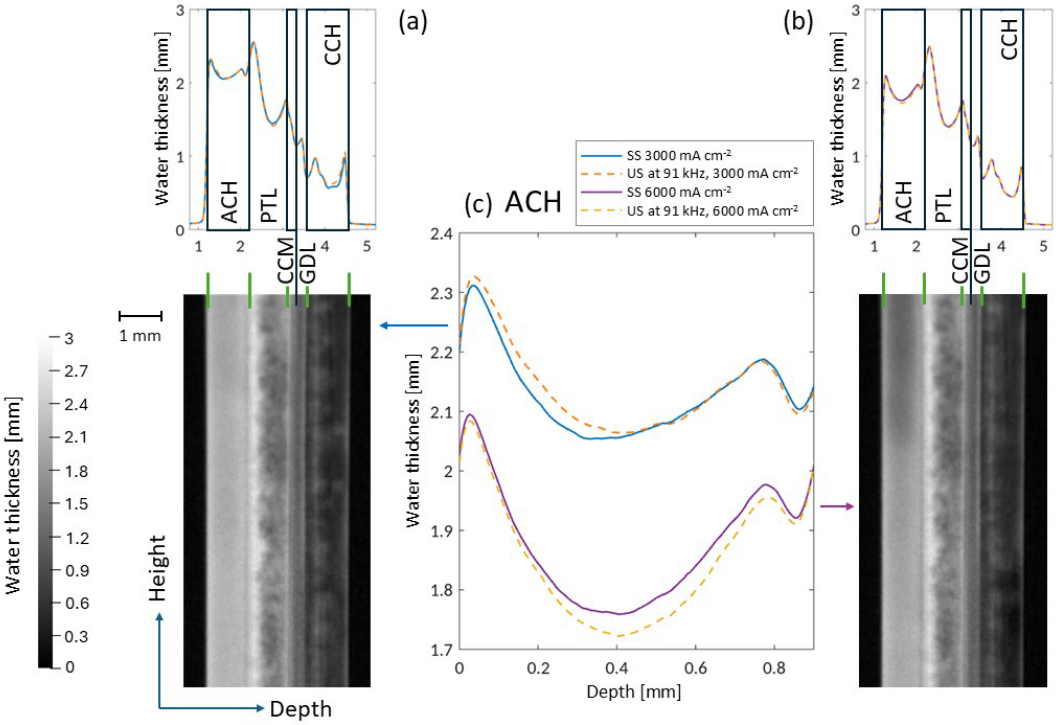

Figure 10. Comparative time-averaged IP water thickness profiles for WE1 for steady-state and US pulsing at 91 kHz and loading power of 7 W cm^{-2} corresponding to 1.92 W cm^{-2} normalized to the whole pulse interval. The test cell was operated at 60°C, water flow rate of 10 ml min^{-1}, and a current density of (a) 3000 mA cm^{-2} and (b) 6000 mA cm^{-2}. (c) Simultaneous plot of the water thickness profiles at the ACH for both current densities during silent and US conditions.

The observed changes in the water thickness might be related to the measured voltage change during US in comparison to its SS value. As already discussed, at current densities up to 3000 mA cm^{-2}, the average voltage during US burst was lower than the voltage in steady state. Based on the water thickness profiles, this could tentatively be attributed to improved two-phase transport in ACH during US pulsing. Operation at higher current density (6000 mA cm^{-2}) resulted in an increase in voltage during US operation despite the measured increase in cell temperature. At the same operating point, a decrease in ACH water thickness was observed. Thus, it could be speculated that the lower water thickness reflected impaired gas removal, which led to increased voltage losses.

CFD-based analysis of two-phase transport in anode channels

Based on the combined modelling and imaging data for the SS regimes, it is evident that higher current densities directly correlate with an increased gas volume occupying the flow channels. Figure 11 presents a comparative analysis of the simulated data, represented by contour plots of gas isosurfaces at a volume fraction of 0.5, and the corresponding processed TP neutron images. This comparison is conducted across six distinct operating conditions, for the two flow rates of 3.25 ml min^{-1} (panels a-c) and 10 ml min^{-1} (panels d-f) and three current densities 1000 mA cm^{-2} (panels a,d), 3000 mA cm^{-2} (panels b,e), 6000 mA cm^{-2} (panels c,f). Within the neutron images, red frames have been added to highlight specific regions indicative of bubble and slug flow structures. It can be deduced that at lower current densities (e.g., 1000 mA cm^{-2} and below), gas evolution primarily results in small, discrete bubbles that occupy a minor fraction of the channel volume. Under these conditions, the application of US is hypothesized to have a positive mass-transport effect. The acoustic field can induce resonant oscillations of bubbles that will lead to microstreaming and bubble coalescence, facilitating bubble detachment from the PTL and enhancing their advection through the channel. Conversely, at elevated current densities combined with low liquid flow rates (e.g., 6000 mA cm^{-2} at 3.25 ml min^{-1}, as shown in panel c), the gas generation rate outpaces the clearing capacity of the flow. This leads to heavy coalescence, resulting in large slug structures that almost entirely occupy the channels. In this specific regime, US may have no or even a detrimental effect

since the acoustic energy could disrupt the transport and the integrity of these large structures, fragmenting them into smaller bubbles.

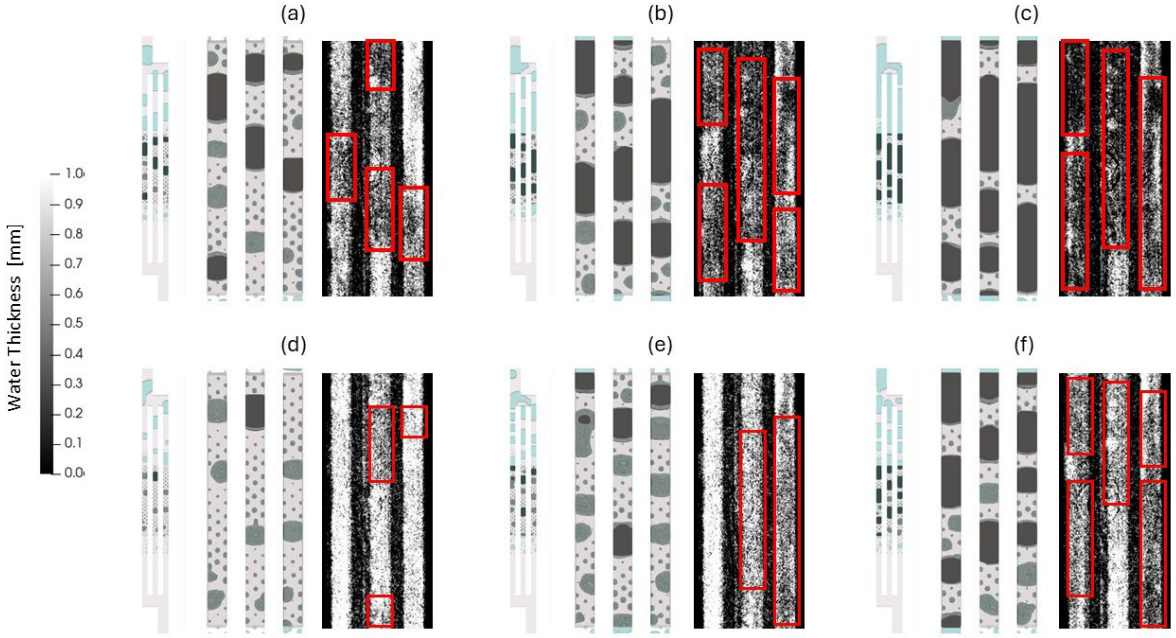

Figure 11. CFD contour plots of isosurfaces with a volume fraction value 0.5, with their corresponding TP images of the operating condition for WE2. The images correspond to steady-state conditions of 30ºC, water flow rates of 3.25 ml min^{-1} (a-c) and 10 ml min^{-1} (d-f) at current densities of 1000 mA cm^{-2} (a,d), 3000 mA cm^{-2} (b,e), and 6000 mA cm^{-2} (c,f). Red frames indicate typical gas slug formations observed.

Conclusions

This study presented a combined experimental and numerical investigation of ultrasound (US) assisted proton exchange membrane water electrolysis (PEMWE), employing operando neutron imaging to quantify multiphase transport phenomena. The neutron radiography measurements enabled spatially resolved determination of water thickness, used here as a proxy for gas distribution, revealing clear modifications of the two-phase flow behaviour under US excitation. The results demonstrate that the impact of the US is strongly dependent on the operating condition. At intermediate current densities (100 mA, 1000 mA, 3000 mA cm^{-2}), US induces a reduction in cell voltage and an increase in water content within the flow channels, indicating enhanced gas removal and improved mass transport conditions. In contrast, at high current densities, a decrease in water content and a corresponding increase in voltage were observed, suggesting a detrimental effect associated with altered two-phase flow structure. The combination of imaging and computational fluid dynamics (CFD) analysis indicates that these opposing trends can be linked to a transition from dispersed bubbly flow to slug-dominated regimes, where US may promote bubble fragmentation or destabilisation of large gas structures. However, the present study does not directly resolve bubble-scale dynamics, and the underlying mechanisms, such as acoustic streaming, rectified diffusion, or cavitation, cannot be distinguished. Although measurable voltage reductions were observed, the energetic cost of US excitation significantly exceeds the electrochemical performance gains under the investigated conditions. The primary contribution of this work lies in understanding the associated phenomena rather than immediate efficiency improvements.

Author contributions

Conceptualization – ST, TM, CDO, TVK, MG; Data curation – ST, TM; Formal analysis – ST, TM; Funding acquisition – TVK, MG, CDO; Investigation – ST, TM, WZ, XM, YZ, JCPK, PV, NK, JH, AT, LH, BL; Methodology - ST, TM, BL, NK, LH, AT; Project administration – TM, CDO, TVK, IK, MG; Resources - TVK, MG, CDO, AT, LH, BL; Software – ST, AG, TA, TM, YF; Supervision – CDO, TVK, IK, MG; Validation – TM, ST, WZ, MG, TVK; Visualization – ST, TM; Roles/Writing - original draft – ST, TM; and Writing - review & editing – WZ, XM, YF, TA, JCPK, PV, NK, IM, JH, AG, AT, LH, BL, CDO, TVK, IK, MG.

Conflicts of interest

The authors declare no conflict of interest.

Data availability

The data supporting this study are available from the Institute Laue-Langevin (ILL) repository[38]. Data processing scripts and analysis code along with CFD case setup are available upon request from the corresponding author.

Acknowledgements

The authors gratefully acknowledge the funding by the European Regional Development Fund (ERDF) within the programme Research and Innovation - Grant Number ZS/2023/12/182138. This research is part of the Research Initiative SmartProSys: Intelligent Process Systems for the Sustainable Production of Chemicals, funded by the Ministry for Science, Energy, Climate Protection, and the Environment of the State of Saxony-Anhalt. This research has also received funding jointly from the UKRI and the EU under HORIZON - Marie Skłodowska-Curie Actions - 2021- DN - 01 Project: 101072851 — MFLOPS.

List of abbreviations

ACH	anode flow channels	LGS	liquid–gas separator
AMP	amplifier	MPI	Max Planck Institute
CCM	catalyst-coated membrane	OCV	open-circuit voltage
CFD	computational fluid dynamics	OER	oxygen evolution reaction
CCH	cathode flow channels	OI	operating image
CH	channel	OS	Oscilloscope
CSF	continuum surface force	P	Pump
DF	dark field	PEMWE	proton exchange membrane water electrolyser
DI	dry image	PG	potentiostat/galvanostat
EIS	electrochemical impedance spectroscopy	PTL	porous transport layer
FG	frequency generator	ROI	region of interest
FIC	flow indicator and controller	SS	steady state
GDL	gas diffusion layer	TC	Thermostat
HFR	high-frequency resistance	TI	temperature indicator
HER	hydrogen evolution reaction	TP	through-plane
ILL	Institut Laue-Langevin	US	Ultrasound
IP	in-plane	V	Valve
L	land	VoF	volume of fluid

Notes and references

1 Suzuki T, Iiyama A, Kubo N, Saito N, Shinohara K, Shimotori S, Sugawara Y, Yamada K. (Invited) Toward the Future Fuel Cell - Challenge for 2040-. *ECS Transactions*. 2019;92(8):3. doi:10.1149/09208.0003ecst

2 Dowling JA, Rinaldi KZ, Ruggles TH, Davis SJ, Yuan M, Tong F, Lewis NS, Caldeira K. Role of Long-Duration Energy Storage in Variable Renewable Electricity Systems. *Joule*. 2020;4(9):1907-1928. doi:10.1016/j.joule.2020.07.007

3 Ruggles TH, Dowling JA, Lewis NS, Caldeira K. Opportunities for flexible electricity loads such as hydrogen production from curtailed generation. *Advances in Applied Energy*. 2021;3:100051. doi:10.1016/j.adapen.2021.100051

4 Marangio F, Santarelli M, Cali M. Theoretical model and experimental analysis of a high pressure PEM water electrolyser for hydrogen production. *International Journal of Hydrogen Energy*. 2009;34(3):1143-1158. doi:10.1016/j.ijhydene.2008.11.083

5 Schmidt G, Suermann M, Bensmann B, Hanke-Rauschenbach R, Neuweiler I. Modeling Overpotentials Related to Mass Transport Through Porous Transport Layers of PEM Water Electrolysis Cells. *J Electrochem Soc*. 2020;167(11):114511. doi:10.1149/1945-7111/aba5d4

6 Trinke P, Keeley GP, Carmo M, Bensmann B, Hanke-Rauschenbach R. Elucidating the Effect of Mass Transport Resistances on Hydrogen Crossover and Cell Performance in PEM Water Electrolyzers by Varying the Cathode Ionomer Content. *J Electrochem Soc*. 2019;166(8):F465-F471. doi:10.1149/2.0171908jes

7 Ojong ET, Kwan JTH, Nouri-Khorasani A, Bonakdarpour A, Wilkinson DP, Smolinka T. Development of an experimentally validated semi-empirical fully-coupled performance model of a PEM electrolysis cell with a 3-D structured porous transport layer. *International Journal of Hydrogen Energy*. 2017;42(41):25831-25847. doi:10.1016/j.ijhydene.2017.08.183

8 García-Salaberri PA. 1D two-phase, non-isothermal modeling of a proton exchange membrane water electrolyzer: An optimization perspective. *Journal of Power Sources*. 2022;521:230915. doi:10.1016/j.jpowsour.2021.230915

9 Schuler T, Schmidt TJ, Büchi FN. Polymer Electrolyte Water Electrolysis: Correlating Performance and Porous Transport Layer Structure: Part II. Electrochemical Performance Analysis. *J Electrochem Soc*. 2019;166(10):F555-F565. doi:10.1149/2.1241908jes

10 Lee CH, Banerjee R, Arbabi F, Hinebaugh J, Bazylak A. Porous Transport Layer Related Mass Transport Losses in Polymer Electrolyte Membrane Electrolysis: A Review. In: *ASME 2016 14th International Conference on Nanochannels, Microchannels, and Minichannels*. American Society of Mechanical Engineers; 2016:V001T07A003. doi:10.1115/ICNMM2016-7974

11 Maier M, Smith K, Dodwell J, Hinds G, Shearing PR, Brett DJL. Mass transport in PEM water electrolysers: A review. *International Journal of Hydrogen Energy*. 2022;47(1):30-56. doi:10.1016/j.ijhydene.2021.10.013

12 Swiegers GF, Terrett RNL, Tsekouras G, Tsuzuki T, Pace RJ, Stranger R. The prospects of developing a highly energy-efficient water electrolyser by eliminating or mitigating bubble effects. *Sustainable Energy Fuels*. 2021;5(5):1280-1310. doi:10.1039/D0SE01886D
13 Tho P, Manasseh R, Ooi A. Cavitation microstreaming patterns in single and multiple bubble systems. *J Fluid Mech*. 2007;576:191-233. doi:10.1017/S0022112006004393
14 Minnaert M. XVI. *On musical air-bubbles and the sounds of running water*. *The London, Edinburgh, and Dublin Philosophical Magazine and Journal of Science*. 1933;16(104):235-248. doi:10.1080/14786443309462277
15 Agrež V, Heidary Z, Gavaises M, Petkovšek R, Ohl CD. Chladni figures reduce ohmic losses in alkaline electrolysis. *Ultrasonics Sonochemistry*. 2026;128:107833. doi:10.1016/j.ultsonch.2026.107833
16 Pollet BG, Foroughi F, Faid AY, Emberson DR, Islam MdH. Does power ultrasound (26 kHz) affect the hydrogen evolution reaction (HER) on Pt polycrystalline electrode in a mild acidic electrolyte? *Ultrasonics Sonochemistry*. 2020;69:105238. doi:10.1016/j.ultsonch.2020.105238
17 Foroughi F, Immanuel Bernäcker C, Röntzsch L, Pollet BG. Understanding the Effects of Ultrasound (408 kHz) on the Hydrogen Evolution Reaction (HER) and the Oxygen Evolution Reaction (OER) on Raney-Ni in Alkaline Media. *Ultrasonics Sonochemistry*. 2022;84:105979. doi:10.1016/j.ultsonch.2022.105979
18 Kardjilov N, Manke I, Hilger A, Strobl M, Banhart J. Neutron imaging in materials science. *Materials Today*. 2011;14(6):248-256. doi:10.1016/S1369-7021(11)70139-0
19 Selamet OF, Pasaogullari U, Spernjak D, Hussey DS, Jacobson DL, Mat M. In Situ Two-Phase Flow Investigation of Proton Exchange Membrane (PEM) Electrolyzer by Simultaneous Optical and Neutron Imaging. *ECS Trans*. 2011;41(1):349-362. doi:10.1149/1.3635568
20 Hoeh MA, Arlt T, Kardjilov N, Manke I, Banhart J, Fritz DL, Ehlert J, Lüke W, Lehnert W. In-Operando Neutron Radiography Studies of Polymer Electrolyte Membrane Water Electrolyzers. *ECS Trans*. 2015;69(17):1135-1140. doi:10.1149/06917.1135ecst
21 De Beer F, Van Der Merwe JH, Bessarabov D. PEM Water Electrolysis: Preliminary Investigations Using Neutron Radiography. *Physics Procedia*. 2017;88:19-26. doi:10.1016/j.phpro.2017.06.002
22 Maier M, Dodwell J, Ziesche R, Tan C, Heenan T, Majasan J, Kardjilov N, Markötter H, Manke I, Castanheira L, Hinds G, Shearing PR, Brett DJL. Mass transport in polymer electrolyte membrane water electrolyser liquid-gas diffusion layers: A combined neutron imaging and X-ray computed tomography study. *Journal of Power Sources*. 2020;455:227968. doi:10.1016/j.jpowsour.2020.227968
23 Zlobinski M, Babic U, Fikry M, Gubler L, Schmidt TJ, Boillat P. Dynamic Neutron Imaging and Modeling of Cationic Impurities in Polymer Electrolyte Water Electrolyzer. *J Electrochem Soc*. 2020;167(14):144509. doi:10.1149/1945-7111/abc83b
24 Ziesche RF, Hack J, Rasha L, Maier M, Tan C, Heenan TMM, Markötter H, Kardjilov N, Manke I, Kockelmann W, Brett DJL, Shearing PR. High-speed 4D neutron computed tomography for quantifying water dynamics in polymer electrolyte fuel cells. *Nat Commun*. 2022;13(1):1616. doi:10.1038/s41467-022-29313-5
25 Altaf H, Milicic T, Vidakovic-Koch T, Tsotsas E, Tengattini A, Kardjilov N, Arlt T, Manke I, Vorhauer-Huget N. Neutron Imaging Experiments to Study Mass Transport in Commercial Titanium Felt Porous Transport Layers. *J Electrochem Soc*. 2023;170(6):064507. doi:10.1149/1945-7111/acd7a8
26 Hirt CW, Nichols BD. Volume of fluid (VOF) method for the dynamics of free boundaries. *Journal of Computational Physics*. 1981;39(1):201-225. doi:10.1016/0021-9991(81)90145-5
27 Roenby J, Bredmose H, Jasak H. A computational method for sharp interface advection. *R Soc open sci*. 2016;3(11):160405. doi:10.1098/rsos.160405
28 Lafmejani SS, Olesen AC, Kær SK. VOF modelling of gas–liquid flow in PEM water electrolysis cell micro-channels. *International Journal of Hydrogen Energy*. 2017;42(26):16333-16344. doi:10.1016/j.ijhydene.2017.05.079
29 Andersson M, Beale SB, Reimer U, Lehnert W, Stolten D. Interface resolving two-phase flow simulations in gas channels relevant for polymer electrolyte fuel cells using the volume of fluid approach. *International Journal of Hydrogen Energy*. 2018;43(5):2961-2976. doi:10.1016/j.ijhydene.2017.12.129
30 Mulbah C, Kang C, Mao N, Zhang W, Shaikh AR, Teng S. A review of VOF methods for simulating bubble dynamics. *Progress in Nuclear Energy*. 2022;154:104478. doi:10.1016/j.pnucene.2022.104478
31 Zhang G, Qu Z. Numerical Investigation of the Performance of a Proton Exchange Membrane Water Electrolyzer under Various Outlet Manifold Structure Conditions. *Materials*. 2024;17(15):3694. doi:10.3390/ma17153694
32 Dang DK, Zhou B. Numerical analysis of bubble behavior in proton exchange membrane water electrolyzer flow field with serpentine channel. *International Journal of Hydrogen Energy*. 2024;88:688-701. doi:10.1016/j.ijhydene.2024.09.145
33 Qin W, Long T, Maarek J, Zaleski S. Three-dimensional numerical study on hydrogen bubble growth at electrode. *International Journal of Multiphase Flow*. 2026;200:105738. doi:10.1016/j.ijmultiphaseflow.2026.105738
34 Brackbill JU, Kothe DB, Zemach C. A continuum method for modeling surface tension. *Journal of Computational Physics*. 1992;100(2):335-354. doi:10.1016/0021-9991(92)90240-Y
35 Falcão DS, Pinto AMFR. A review on PEM electrolyzer modelling: Guidelines for beginners. *Journal of Cleaner Production*. 2020;261:121184. doi:10.1016/j.jclepro.2020.121184
36 Li SD, Wang CC, Chen CY. Water electrolysis in the presence of an ultrasonic field. *Electrochimica Acta*. 2009;54(15):3877-3883. doi:10.1016/j.electacta.2009.01.087
37 Araújo F, Neto RC, Moita AS. Alkaline water electrolysis: Ultrasonic field and hydrogen bubble formation. *International Journal of Hydrogen Energy*. 2024;78:594-603. doi:10.1016/j.ijhydene.2024.06.263
38 Tamara Miličić, Tobias Arlt, Jayanath C. P. Koliyadu, Yuzhe Fan, Manolis Gavaises, Lukas Helfen, Jakobus Hoffman, Nikolay Kardjilov, Bratislav Lukić, Xiaotong Ma, Claus-Dieter Ohl, Stratis Trachanias, Patrik Vagovic, Tanja Vidaković-Koch, Wenyu Zhao. Ultrasound-enhanced Water Electrolysis: Operando Neutron Imaging Study. Published online 2025:Institut Laue-Langevin (ILL). doi:10.5291/ILL-DATA.1-06-80

